Nature of the Mesoscale Boundary Layer Height and Water Vapor Variability Observed 14 June 2002 during the IHOP_2002 Campaign

F. COUVREUX AND F. GUICHARD

GAME-Meteo-France/CNRS-CNRM/GMME, Toulouse, France

P. H. AUSTIN

Atmospheric Science Programme, Department of Earth and Ocean Sciences, University of British Columbia, Vancouver, British Columbia, Canada

F. CHEN

National Center for Atmospheric Research, Boulder, Colorado

(Manuscript received 4 September 2007, in final form 23 June 2008)

ABSTRACT

Mesoscale water vapor heterogeneities in the boundary layer are studied within the context of the International H_2O Project (IHOP_2002). A significant portion of the water vapor variability in the IHOP_2002 occurs at the mesoscale, with the spatial pattern and the magnitude of the variability changing from day to day. On 14 June 2002, an atypical mesoscale gradient is observed, which is the reverse of the climatological gradient over this area. The factors causing this water vapor variability are investigated using complementary platforms (e.g., aircraft, satellite, and in situ) and models. The impact of surface flux heterogeneities and atmospheric variability are evaluated separately using a 1D boundary layer model, which uses surface fluxes from the High-Resolution Land Data Assimilation System (HRLDAS) and early-morning atmospheric temperature and moisture profiles from a mesoscale model. This methodology, based on the use of robust modeling components, allows the authors to tackle the question of the nature of the observed mesoscale variability. The impact of horizontal advection is inferred from a careful analysis of available observations. By isolating the individual contributions to mesoscale water vapor variability, it is shown that the observed moisture variability cannot be explained by a single process, but rather involves a combination of different factors: the boundary layer height, which is strongly controlled by the surface buoyancy flux, the surface latent heat flux, the early-morning heterogeneity of the atmosphere, horizontal advection, and the radiative impact of clouds.

1. Introduction

Water vapor variability was the main focus of the International H_2O Project (IHOP_2002), which took place in May–June 2002 over the southern Great Plains of the United States (Weckwerth et al. 2004). This field project gathered together most of the techniques for measuring water vapor. We address water vapor variability at the mesoscale (scales larger than thermals, ranging from tens to a few hundreds of kilometers). Comparatively few investigations have considered this scale of variability, mainly because of the lack of observations. Milford et al. (1979), using observations from an instrumented glider, first underscored the variability of water vapor at the mesoscale, which they found to be larger than the variability of either potential temperature or vertical velocity. Mahrt (1991), analyzing aircraft in situ measurements at 300 m above ground level, found that the mesoscale variability of water vapor exceeded the submesoscale variability.

Mesoscale water vapor variability has been stressed as an important condition for convection. Crook (1996), Wulfmeyer et al. (2006), and Stirling and Petch (2004) have shown that the initiation of convection is strongly tied to the accurate estimate of water vapor within the boundary layer (BL). In the latter study, the authors demonstrated that the existence of moisture fluctuations accelerates the initiation of deep convection by 1–3 h, and that convective initiation was most sensitive

Corresponding author address: F. Couvreux, GAME-Meteo-France/CNRS-CNRM/GMME, 42 av. G. Coriolis, 31057, Toulouse CEDEX 1, France.
E-mail: fleur.couvreux@meteo.fr

DOI: 10.1175/2008MWR2367.1

TABLE 1. List of symbols used in the definition of the different length scales, L_{Rau}, L_{wm}, and L_{Rau2}.

Symbol	U	z_i	w_*	Te	θ_o	$w'\theta'_{\mathrm{sfc}}$
	Boundary layer wind speed	Depth of the convective boundary layer	Deardorff convective velocity scale	Time of boundary layer growth	Boundary layer potential temperature	Surface sensible heat flux

to BL moisture fluctuations. They also showed that the horizontal scale of moisture fluctuations should be greater than 10 km in order to have the strongest impact on convective initiation.

Heterogeneous surface characteristics have been identified as one potential cause of mesoscale variability. These heterogeneities have been partitioned into two categories: "fixed" heterogeneities that are related to surface characteristics such as elevation, soil texture, or land cover, and transient heterogeneities such as soil moisture that are strongly modulated by precipitation (Chen et al. 2001; Trier et al. 2004; Holt et al. 2006). It has been difficult to assess the impact of either fixed or transient surface heterogeneity because of the scarcity of measurements: local surface flux measurements can suffer from a lack of representativeness that limits their use at the mesoscale (André et al. 1990). Although satellites may provide some estimates at the large scale, it has been more common to use idealized studies to analyze the impact of surface flux heterogeneities on boundary layer characteristics and convective initiation (Anthes 1984; Avissar and Schmidt 1998; Rabin et al. 1990; Pielke 2001 for a review). Avissar and Schmidt (1998) and André et al. (1990) have shown that only scales of heterogeneity greater than 5–10 km can generate a coherent atmospheric response at the mesoscale. Recently, Kang et al. (2007) used variance decomposition and cospectra to document water vapor variability at scales of 1–20 km from aircraft observations during 5 days of IHOP_2002 and found that for 2 of these days surface heterogeneity could generate mesoscale circulations in convective boundary layers.

More generally, Mahrt (2000) analyzed different scales of heterogeneity that can affect the convective boundary layer. He defined three length scales used at the mesoscale: (i) a convective length scale L_{Rau} first proposed by Raupach and Finnigan (1995), where $L_{\mathrm{Rau}} = (CUz_i)/w_*$ with $C = 0.8$ (see Table 1 for symbols); (ii) a minimum horizontal length scale for the influence of surface heterogeneities derived from the thermal blending height, $L_{\mathrm{wm}} = C_{\mathrm{wm}} z(U\theta_o)/(\overline{w'\theta'_{\mathrm{sfc}}})$, with $C_{\mathrm{wm}} = 3 \times 10^{-3}$; and (iii) a larger horizontal scale, L_{Rau2}, where $L_{\mathrm{Rau2}} = \mathrm{Te}U$ for which surface heterogeneities influence the BL with Te the time of the boundary layer growth. In the present study, considering $U = 5\ \mathrm{m\ s^{-1}}$, $z_i = 1000$ m, $w^* = 1\ \mathrm{m\ s^{-1}}$, $\theta_o = 300$ K, Te = 5 h, and $\overline{w'\theta'_{\mathrm{sfc}}} = 200\ \mathrm{W m^{-2}}$ ($0.1645\ \mathrm{K\ m\ s^{-1}}$), these three length scales equal $L_{\mathrm{Rau}} = 4$ km, $L_{\mathrm{wm}} = 45$ km, and $L_{\mathrm{Rau2}} = 90$ km. Accordingly, 4 km is the finest resolution analyzed here.

Atmospheric conditions compete with surface heterogeneity to influence mesoscale water vapor variability. Findell and Eltahir (2003) underlined the importance of the state of the atmosphere in determining the potential influence of the land surface on convective triggering. Alapaty et al. (1997) used a 1D soil–vegetation–BL model to analyze the impact on BL (e.g., turbulent fluxes, structure, and height) of varying surface characteristics (e.g., soil texture, soil humidity, stomatal resistance, leaf area index, and vegetation cover). The greatest influence was found from the first three parameters. Desai et al. (2006) also studied the impact of soil moisture on the boundary layer height variability using a one-dimensional boundary layer model. They found that soil moisture has a strong impact on buoyancy flux that in turn is the primary driver of boundary layer height variability. Here we use a similar approach, focusing on the boundary layer water vapor variability.

We begin by documenting the boundary layer height and the water vapor variability at the mesoscale observed during IHOP_2002. During 14 June 2002, a significant mesoscale gradient of the BL water vapor was observed. A boundary layer bulk model using inputs from a high-resolution land data assimilation system and a mesoscale simulation is used to investigate and quantify the role of early-morning atmosphere and surface fluxes heterogeneity on such variability.

Section 2 presents the data and the methodology, followed by an evaluation of each component of the approach. In section 3, the case study, which is characterized by the strongest mesoscale variability observed during IHOP_2002 is presented. Section 4 evaluates the impact of surface flux heterogeneities, early-morning atmospheric profiles, and advection as sources of mesoscale variability.

2. Methodology

Fully coupled surface–atmospheric mesoscale models are powerful tools for the study of land–atmosphere interactions. Their representations of moist processes, cloud cover, and surface fluxes are however still incom-

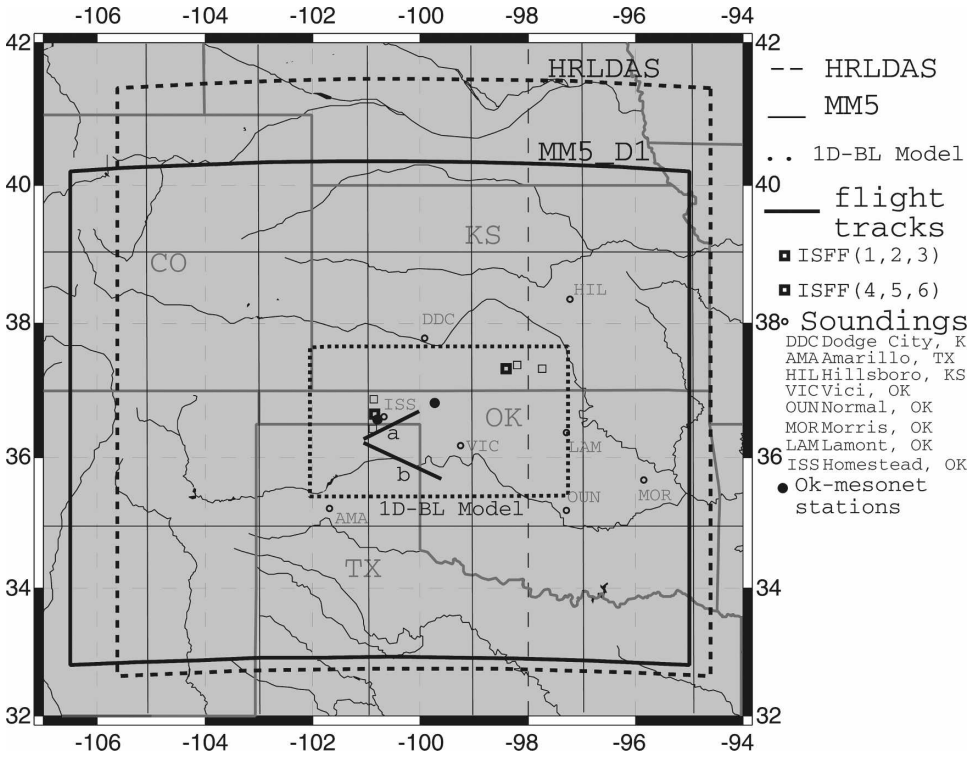

FIG. 1. Map of the domain of interest with the simulation domain for MM5 and HRLDAS and the location of soundings, surface stations, and flight tracks of the Navy P-3 for the northernmost track, noted "a", and of the DLR Falcon for both tracks, noted "a" and "b."

plete (e.g., Betts 2004), and the nonlinear coupling between surface and atmosphere makes it difficult to isolate individual physical processes affecting boundary layer heterogeneity. The alternative and complementary approach employed in section 2b is to study the evolution of an observed BL with mesoscale variability using a collection of 1D models. The BL models are initialized with heterogeneous atmospheric fields provided by a mesoscale model and with surface fluxes calculated by a soil–vegetation–atmosphere transfer (SVAT) model. This framework allows separating the effect of heterogeneity of surface forcing and early-morning atmospheric conditions, permitting a direct comparison of their respective impacts on the development and maintenance of water vapor variability at the mesoscale.

a. Data

We focus primarily on the observations made during the boundary layer evolution IOP of 14 June 2002 documented in the vicinity of Homestead, Oklahoma. We also make use of observations available for 12 and 13 June 2002, in order to provide a better understanding of the synoptic situation. The focus area is indicated in Fig. 1 (which will be referred to as the 1D BL model domain): the domains used for the SVAT [the High-Resolution Land Data Assimilation System (HRLDAS) model described in section 2b)] and the fifth-generation Pennsylvania State University–National Center for Atmospheric Research Mesoscale Model (MM5) are also shown. The 1D BL model domain is about 500 km × 200 km.

Nine surface flux stations [referred to as the Integrated Surface Flux Facility (ISFF)] were installed during IHOP_2002 (LeMone et al. 2007); they are used to evaluate the land surface model. Oklahoma mesonet surface stations, radiosondes from the National Weather Service network, from the Atmospheric Radiation Measurement Program (ARM) southern Great Plains (SGP) network and the specific soundings deployed for IHOP_2002 are used to document the mesoscale variability. In addition, in situ aircraft measurements from the Naval Research Laboratory P-3 (P-3) and the University of Wyoming King Air (UWKA) that flew from 0700 to 1400 Local Daylight Time (LDT) 14 June 2002 (1200–1900 UTC; UTC = LDT + 5) sampled the horizontal variability within the boundary layer. Boundary layer heights are derived from reflectivity profiles measured by the lidar on board the DLR-Falcon, following Davis et al. (2000). The precipi-

tation field is provided by the National Centers for Environmental Prediction (NCEP) stage IV rainfall product, at 4-km resolution, which combines Oklahoma Mesonet rain gauge observations and hourly precipitation radar data.

The Moderate Resolution Imaging Spectroradiometer (MODIS) installed on *Terra*, a sun-synchronous polar-orbiting satellite provides measurement of the precipitable water (PW), a vertically integrated quantity. The MODIS MOD07 PW products are calculated for both day and nighttime orbits at 5×5 km^2 resolution (Seemann et al. 2003; King et al. 2003). The use of MODIS PW is motivated by the analysis presented as follows, where we first establish the role of low-level water vapor in the variability of PW using radiosoundings. Figure 2a shows the variation of the total PW and the contribution of the low levels (<2000 m) for all the soundings measured from 12 to 14 June 2002. The low-level water vapor contributes significantly to PW; for more than 65% of the soundings, 70% of the PW is located below 2000 m. In addition, PW fluctuations are dominated by the variability of the low levels. Boundary layer water vapor mixing ratio and PW are strongly linked (Fig. 2b, $r^2 = 0.74$). Thus, PW appears to be a good tracer of BL water vapor variability.

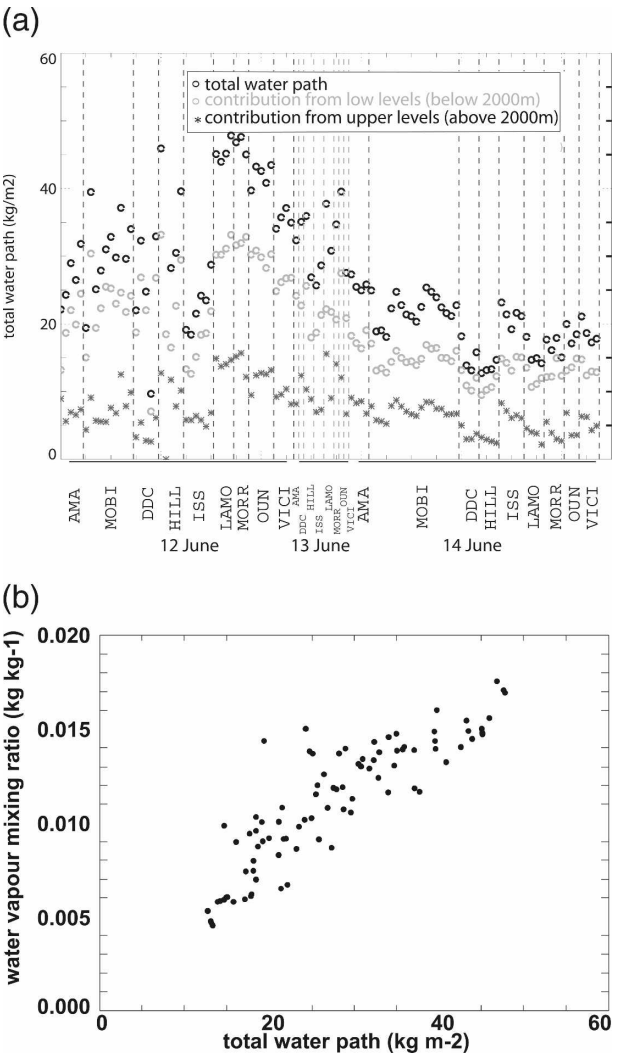

FIG. 2. (a) Variations, for the period of interest, of the total water path (kg m^{-2}) (black circles), contribution from the low levels (below 2000 m, gray circles), and contribution from the upper levels (above 2000 m, black stars); (b) scatterplot of mean q in low levels as a function of the total water path. The soundings are indicated in Fig. 1 (except MOBI that corresponds to the mobile soundings).

b. Models description

We use a 1D boundary layer model with, as lower boundary conditions, the surface fluxes, provided by HRLDAS and initial atmospheric profiles provided by MM5. This model predicts the development of the convective boundary layer from the early-morning profiles using time-varying surface fluxes. As noted in section 1, mesoscale variability is not sensitive to horizontal structure below the 4-km convective length scale L_{Rau}, which also matches the 4-km horizontal resolution of HRLDAS. Model columns are treated independently on the 1D BL model domain, ignoring mesoscale circulations; analysis of the MM5 simulation performed for this day indicates that the mesoscale circulations are weak.

1) THE MIXED LAYER SLAB MODEL

This model (henceforth the "BL model") is a mixed layer slab model, based on the zero-order jump approximation, which characterizes the convective boundary layer by its mean depth h, the height-independent mean potential temperature θ_m, and the height-independent water vapor mixing ratio q_m. The surface fluxes are prescribed by HRLDAS. The closure involves a parameterized form of the entrainment buoyancy flux. Here, we assume that the entrainment flux is a constant fraction c of the surface flux with $c = -0.2$ (Stull 1988). The BL model details are given in the appendix.

The BL model has been evaluated against nine different cases (initial profiles shown in Fig. 3, top panels) covering the range of environmental conditions encountered during the focus period via systematic comparisons with large-eddy simulations of the same cases (Couvreux et al. 2005, hereafter C05; Couvreux et al. 2007, hereafter C07; for information on the design of these LES). The nine cases are aimed at testing the ability of the BL model to represent the properties of the convective BL during its daytime growth under

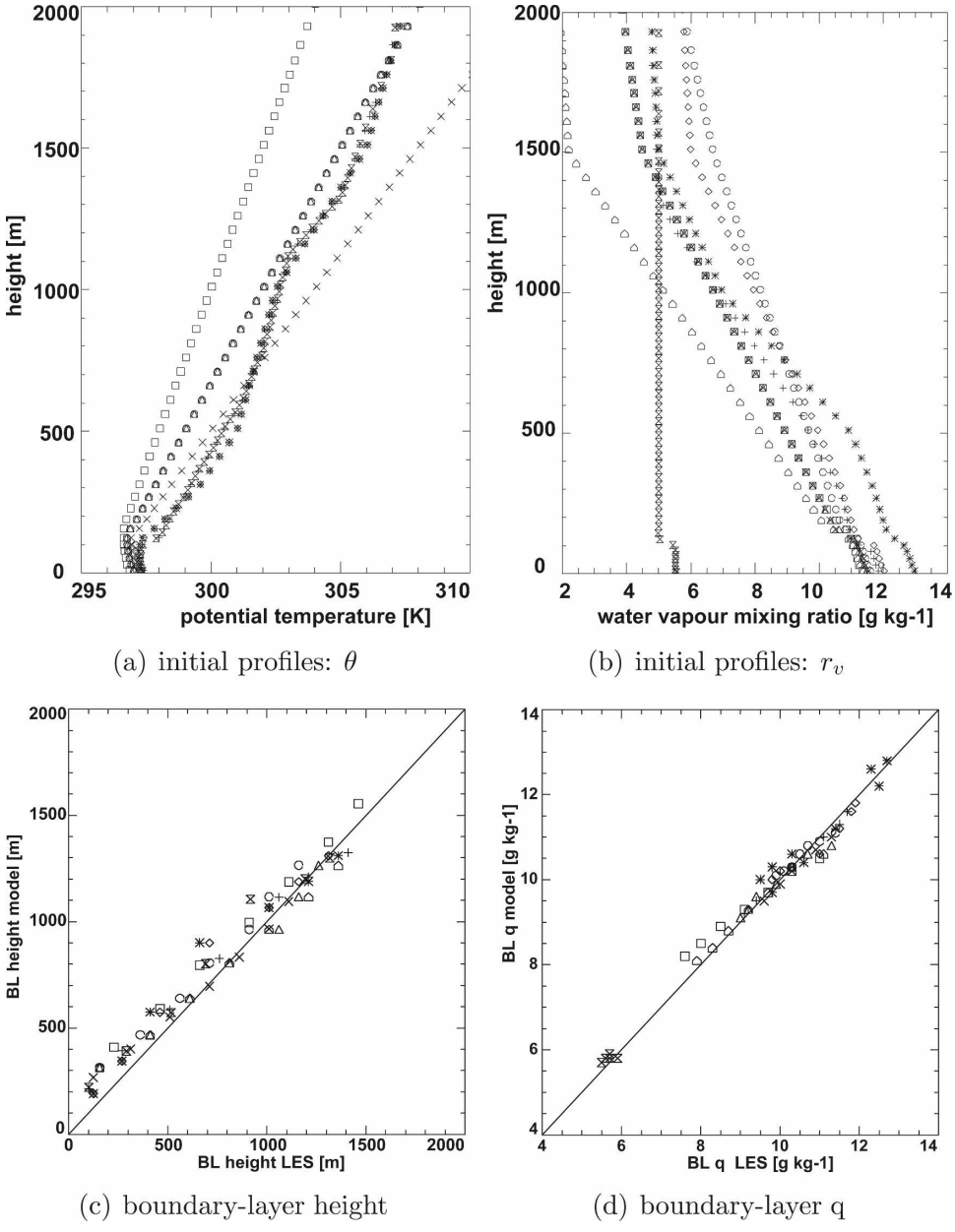

FIG. 3. Initial profiles of (a) potential temperature and (b) water vapor mixing ratio for the nine simulations used to evaluate the BL model. Evaluation of the model against LES for the nine 7-h-long simulations (a symbol is drawn for each hour, from 0700 to 1400 LDT): (c) boundary layer height and (d) boundary layer water vapor mixing ratio.

varying environmental conditions, therefore the cases only differ by their initial profiles, namely their lapse rate and mixing ratio profiles. The runs lasted for 7 h starting at 0700 LDT. Both h and q_m are compared to values obtained by LES (Fig. 3, bottom panels). The BL model satisfactorily predicts the time evolution of the mixed layer characteristics. Although a more complex boundary layer model could be used, this simple model represents the basic features of a developing convective boundary layer with sufficient accuracy for our purpose.

2) HRLDAS MODEL

HRLDAS (Chen et al. 2007) employs the Noah land surface model and is run in uncoupled mode (not coupled to an atmospheric model) on a 4-km grid for an 18-month spinup period starting 1 Jan 2001, so that the

soil profiles used in this June 2002 case are physically reasonable. The land surface initialization uses a variety of observed and analyzed conditions including 1) NCEP stage IV rainfall data (discussed in section 2a) on a 4-km national grid; 2) 0.5° hourly downward solar radiation derived from the *Geostationary Operational Environmental Satellites* (*GOES-8* and *GOES-9*); 3) near-surface atmospheric temperature, humidity, wind, downward longwave radiation, and surface pressure from 3-hourly NCEP Environmental Data Assimilation System (EDAS) analyses; 4) 1-km horizontal resolution U.S. Geological Survey 24-category land-use and 1-km horizontal resolution state soil geographic soil texture maps; and 5) 0.15° monthly satellite-derived green vegetation fraction. As shown in Drusch and Viterbo (2007), it is premature to use soil moisture as an input for land surface initialization.

This soil initialization system (HRLDAS) was evaluated by Chen et al. (2007) using IHOP_2002 ISFF and Oklahoma Mesonet data along the IHOP_2002 period. Here, we evaluate HRLDAS in more detail for the period from 12 to 14 June. The soil temperature and humidity are consistent with the values observed at the six ISFF stations located in the BL model domain. The increase of soil moisture following the 13 June rain events is greater in the south than the north, consistent with the gradient in rainfall amounts. HRLDAS soil moisture has also been compared for these 3 days to the soil moisture derived from the Tropical Rainfall Measuring Mission (TRMM) Microwave Imager (TMI) brightness temperatures (Gao et al. 2006). After accounting for the difference in resolution, HRLDAS and TMI soil moisture maps display qualitatively similar patterns (Figs. 4b–d), with a dry anomaly in the northwest persisting over the 3 days and wet anomalies strongly linked to the spatial structure of the cumulative precipitation field for the precipitation events described below in section 3. The amplitude of the soil moisture fluctuations is smaller in HRLDAS (0.09, 0.34 $m^3\ m^{-3}$) than in the TMI retrieval (0.04, 0.48 $m^3\ m^{-3}$). The smaller range is at least partly explained by the shallow (0.5 cm) sampling depth of the TMI compared to the 0–10-cm first soil layer of HRLDAS. Note particularly that TMI records a higher and more confined maximum in the southwest corner than HRLDAS. Soil texture patterns (Fig. 4f) also influence HRLDAS soil moisture, as shown by the sandy soil footprint evident in soil moisture structures.

An evaluation of HRLDAS surface fluxes using ISFF measurements is not always straightforward simply because ISFF and HRLDAS provide distinct fields: specifically the ISFF yields a local flux measurement whereas the HRLDAS represents a $4 \times 4\ km^2$ horizontal mean. Here, we focus on the consistency of both datasets at two stations, ISFF-2 and ISFF-4 (Fig. 1), located, respectively, within crop/grassland and grassland zones. Figure 5 shows the time evolution of daytime H (left panels), LE (middle panels), and total surface heat flux (right panels) for these two stations. Both stations recorded similar radiation but with a larger sensible heat flux (H) for station 2 and a larger latent heat flux (LE) for station 4 (the rainfall accumulation during the period of interest was 7 times larger at ISFF-4 than at ISFF-2). HRLDAS is able to represent the main differences between these two stations. However, LE differs more than H between HRLDAS and ISFF (with smaller values for ISFF), even though Rnet $- G - H$ (where Rnet is the net radiation and G the ground heat flux) in ISFF and HRLDAS are in closer agreement. This apparent overestimation of LE by HRLDAS is however consistent with the frequently reported underestimation of surface fluxes by eddy-correlation methods (e.g., Brotzge and Crawford 2003; Chen et al. 2007). Indeed, there is better agreement between H + LE in HRLDAS and Rnet $- G$ measured by ISFF. Such an underestimation occurs more often during days following important precipitation events (LeMone et al. 2007) like 14 June. Nevertheless, there is a general agreement between the time evolution of the ISFF-measured heat fluxes and those predicted by HRLDAS. Moreover, HRLDAS is able to reproduce the Bowen ratio observed at these stations (not shown), indicating a good simulation of the partitioning of Rnet between H and LE.

For this period, which experienced significant precipitation, HRLDAS predictions benefited in particular from the strong constraint on cumulative precipitation provided by the NCEP stage IV rainfall product. In fact forcing a land surface scheme with such analysis restrains the errors introduced by surface–atmosphere coupling in atmospheric models, which often have biases in their prediction of precipitation and other fields (Betts and Jakob 2002).

3) INITIAL ATMOSPHERIC PROFILES FROM MM5

MM5 (Grell et al. 1995), version 3, has been used to initialize the BL model at 0800 LDT by gridded early-morning atmospheric profiles. The simulation starts at 0700 LDT 14 June 2002 from the NCEP Eta analysis. Note that HRLDAS was not used to initialize the mesoscale model. Given the very weak early-morning surface fluxes, using a different surface flux parameterization is not expected to impact much the calculation of the 0800 LDT atmosphere stratification. The MM5 domain is shown in Fig. 1; it is simulated with a horizontal

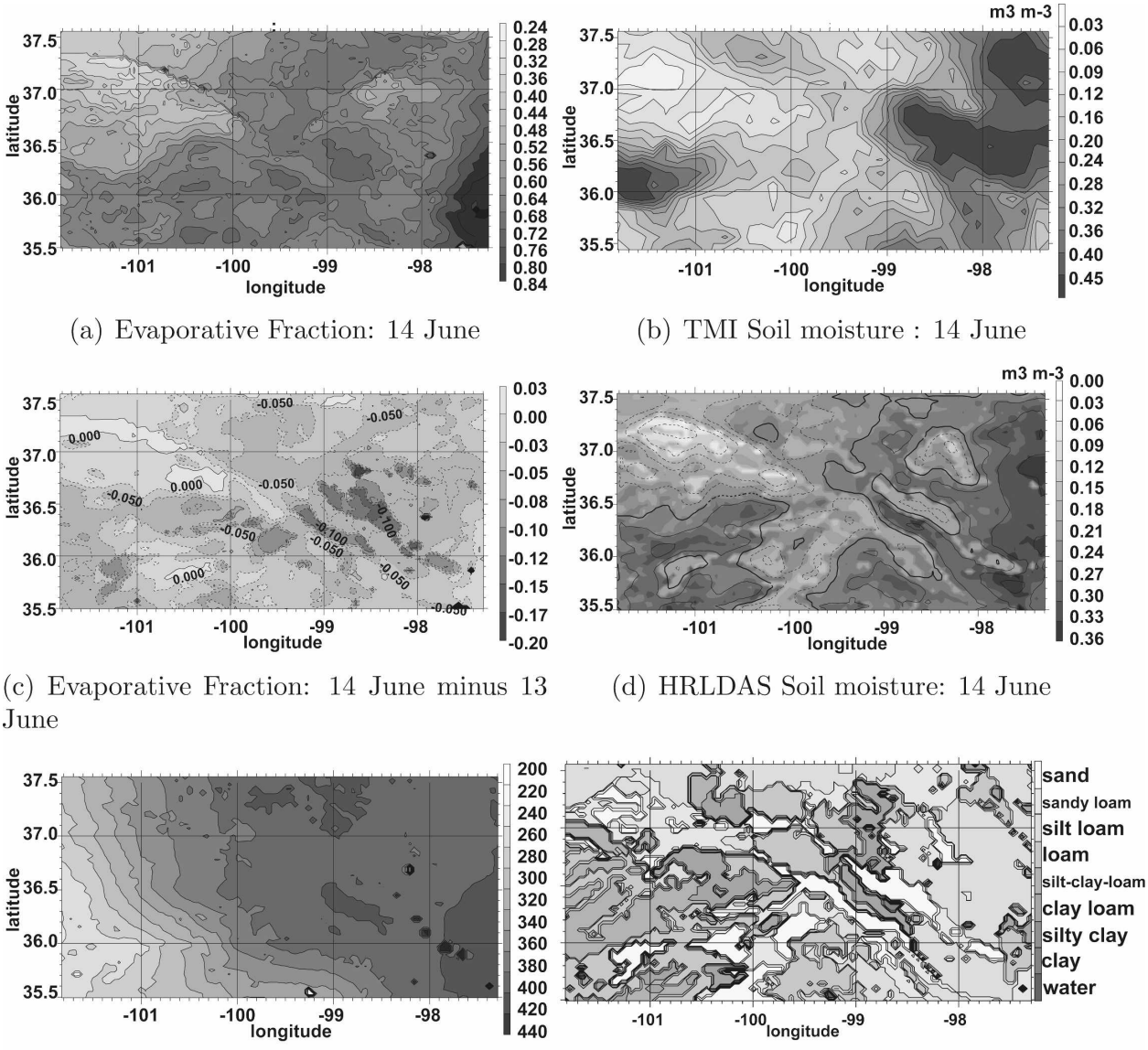

(a) Evaporative Fraction: 14 June

(b) TMI Soil moisture : 14 June

(c) Evaporative Fraction: 14 June minus 13 June

(d) HRLDAS Soil moisture: 14 June

(e) Latent plus Sensible Heat Fluxes: 14 June

(f) HRLDAS Soil texture

FIG. 4. (top left) The Ef computed from cumulative surface flux from 0600 to 1800 LDT 14 Jun, (middle left) the cumulative Ef difference between 13 and 14 Jun, (bottom left) latent plus sensible heat flux averaged from 0600 to 1800 LDT 14 Jun, (top right) TMI soil moisture for 14 Jun, (middle right) HRLDAS soil moisture (the isolines, every 0.03 m^3 m^{-3} with negative values in dashed, correspond to the anomalies retrieved at a similar resolution as TMI), and (bottom right) HRLDAS soil textures. HRLDAS fields (fluxes and soil moisture) are available at a 4-km resolution whereas TMI has a 12 km × 15 km resolution.

resolution of 12 km. A sensitivity test with a 4-km horizontal resolution on a smaller domain (35.5°–37.6°N, −102.4° to −99.5°W) demonstrated that increasing the horizontal resolution had no significant impact on the resulting atmospheric profiles. Figure 6 shows the comparison to radiosoundings at five locations noted in Fig. 1. The mesoscale model correctly simulates the early-morning general structure of the atmosphere. In particular the lapse rate and the q profile are well reproduced, as is the observed range of variability. MM5 does not, however, capture the vertical stratification of the mixing ratio observed by radiosoundings.

3. The 14 June case study: A nonclimatological humidity gradient

a. Mesoscale variability and climatology

The choice of the case study was motivated by the strongest observed mesoscale variability in IHOP_2002 aircraft data and the atypical moisture gradient.

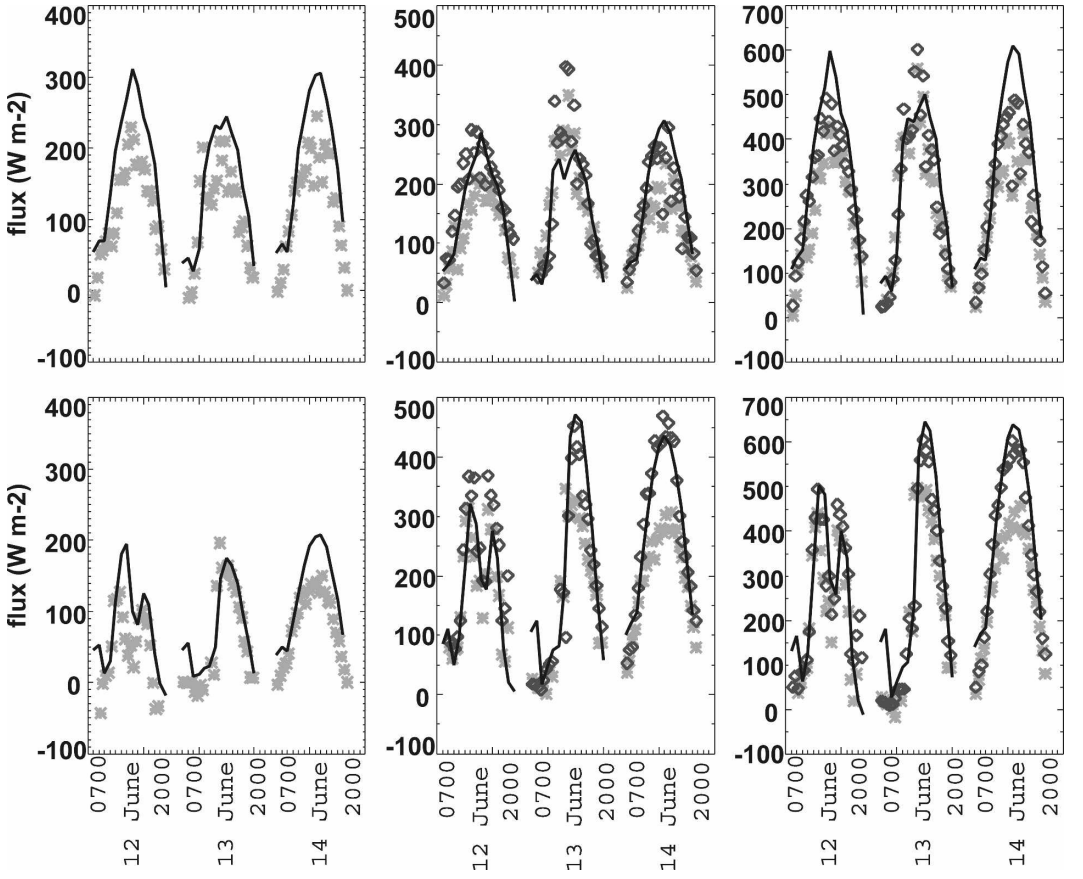

FIG. 5. Comparison of daytime surface fluxes predicted by HRLDAS hourly (black) and observed at the ISFF station semihourly (gray stars) for 12, 13, and 14 Jun 2002: (top) ISFF-2 and (bottom) ISFF-4, (left) sensible heat flux, (middle) latent heat flux, and (right) sensible plus latent heat flux. The dark gray diamonds correspond to the latent heat flux computed as a residual Rnet $-$ G $-$ H on the middle panels and to Rnet $-$ G on the right panels.

1) MESOSCALE VARIABILITY ALONG IHOP_2002 INFERRED FROM AIRCRAFT IN SITU DATA

Water vapor mixing ratio variability is investigated using a total of 35 h of the UWKA aircraft data divided into 148 legs with an average leg length of 50 km at different vertical levels sampled over 14 days. "Boundary layer heterogeneity" flights consisted of successive legs at different altitudes from 65 m above the surface to the upper boundary layer while during "boundary layer evolution" flights the aircraft flew at one or two constant altitudes in the lower half of the BL (Weckwerth et al. 2004). Since we focus on the mesoscale we filter the 1-Hz (90 m) aircraft measurements with a 10-km running mean.

For these flight tracks, the mesoscale fluctuations vary from day to day while the submesoscale (scales smaller than 10 km) variability, which is caused primarily by the boundary layer dynamics, remains of the same order of magnitude on the different days (C07). The sampled mesoscale variability in the lower half of the BL is greatest on 14 June, with a standard deviation for each leg varying from 0.5 to 0.8 g kg^{-1}. This is larger than the submesoscale standard deviation on this day, which is about 0.2 g kg^{-1}. The single-leg standard deviations vary from 0.3 to 0.6 g kg^{-1} for 29 and 30 May to less than 0.4 g kg^{-1} for the other days. Note that normalizing this standard deviation by the length of the leg slightly decreases the difference between 14 June (longest legs) and the other days, but 14 June still records the largest mesoscale variability.

2) COMPARISON TO CLIMATOLOGY

The water vapor climatology in the IHOP_2002 domain is characterized by a horizontal gradient in water vapor with drier air to the west and moister air to the east (Dodd 1965). A strong east–west gradient in rainfall is also typical for this area (Weckwerth et al. 2004). During the IHOP_2002 field campaign, the cumulative rainfall from 10 May to 25 June was about 70 mm for

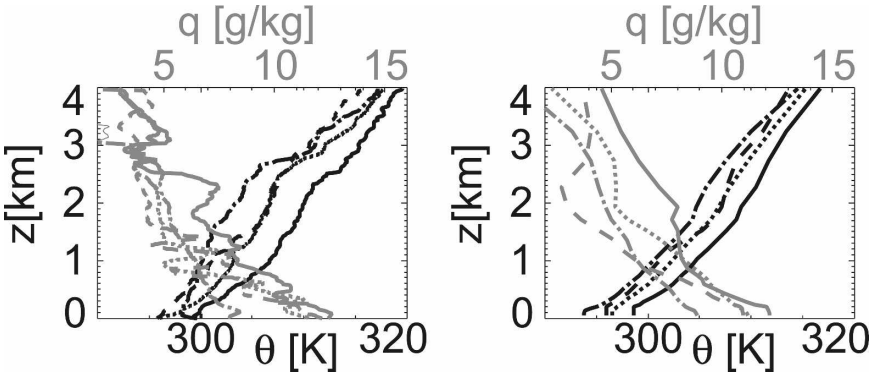

FIG. 6. Vertical profile of θ (black) and q (gray) (a) observed by radiosoundings and (b) simulated by MM5 at Amarillo (full line), Homestead, ISS (dotted line), Vici (dashed line), and Dodge City (dot–dashed line) on early morning 14 Jun 2002.

ISFF-3 (36.9°N, −100.6°W), 170 mm for ISFF-5 (37.4°N, −98.2°W), and 300 mm for ISFF-8 (37.4°N, −96.8°W; LeMone et al. 2007). A gradient is also evident in the mean PW for June 2002 computed from the 40-yr European Centre for Medium-Range Weather Forecasts (ECMWF) Re-Analysis (ERA-40), with values lower than 30 kg m^{-2} west of 101°W, and a maximum located on the southeastern part of the domain with values greater than 34 kg m^{-2}. A similar gradient characterizes the mean PW over the area in June from 1992 to 2002 (Fig. 8c). There are, however, day-to-day departures from climatology. From 1992 to 2002, on average, 4 days in June were characterized by an inverse (westward increasing) moisture gradient. Typically this inverse gradient is accompanied by a small domain-averaged value of PW and high surface pressure. The 14 June case is an example of one of those atypical days. It shares the same features, low PW (Fig. 2 from soundings and Fig. 8d from ERA-40) and large mean surface pressure exceeding 1020 hPa.

b. Overview of the 12–14 June period

This period follows 3 days dominated by southerly advection of moisture from 8 to 11 June. From 12 to 14 June, a low pressure center moved from the border between Saskatchewan, Canada, and Montana on 12 June to Minnesota on 14 June. This circulation brought dry and relatively cool air: inspection of ERA-40 reanalysis (PW and horizontal winds) indicates advection of dry air on the northeastern part of the domain. Advection is less important to the northwest due to an anticyclonic circulation present on 14 June over this area. By bringing dry air into the northeast of the domain, this advection tends to strengthen the observed mesoscale gradient. On 14 June, no large-scale boundaries (such as fronts or drylines) are evident.

Three precipitation events occurred over the selected area from 11 to 13 June. The first was associated with a convective system that originated in Colorado, and brought precipitation over the northeastern part of the domain up to 0900 LDT 12 June. The second one developed in the late afternoon of 12 June: numerous convective cells developed slightly south of the cold front present over the area. Most of the precipitation fell on the central part of the domain. On 13 June, a mesoscale convective system initiated over Colorado moved over the area bringing precipitation mainly to the south of the domain. According to Wilson and Roberts (2006), 12–13 June was a convectively active period. These events deposited precipitation over the area heterogeneously. More rainfall was received in the southwest and less in the northwest of the domain. This is illustrated in the soil moisture content observed by TMI 14 June 2002 (Fig. 4b).

Both LE and rainfall at the three western ISFF are shown in Fig. 7. On 13 June, LE is the highest (about 370 W m^{-2} as maximum around midday) at ISFF-1 where more rainfall (35 mm) was received. There is an approximately 80 W m^{-2} difference between the maximum LE at ISFF-1 and ISFF-2 at noon. This difference diminishes progressively during the 13 June afternoon and 14 June, indicating that after a day the LE contribution due to the rainfall difference has decreased considerably. The evaporative fraction (Ef; ratio of LE over H + LE, not shown) also reflects the difference after rain in the three ISFF with larger values (0.8 on 13 June and 0.7 on 14 June) for ISFF-1, than ISFF-2 (0.65 on 13 June and 0.6 on 14 June) and ISFF-3 (about 0.4 for both days). The LE morning maximum for 13 June at ISFF-3 seems to be caused by an afternoon increase of cloudiness.

For the three days, Ef in HRLDAS shows patterns at

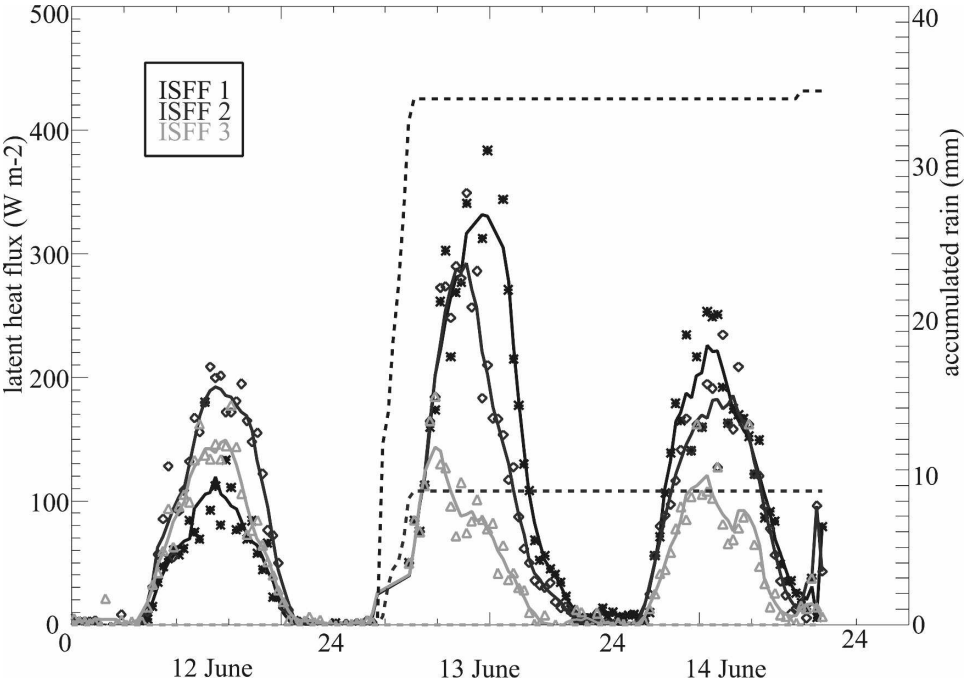

FIG. 7. Temporal evolution (semihourly) of surface latent heat flux (symbols, the line correspond to the evolution averaged with a running-mean of 2 h) and cumulative precipitation (dashed line) over ISFF-1 (black lines and stars; 36.5°N, 100.6°W), ISFF-2 (dark gray lines and diamonds; 36.6°N, 100.6°W), and ISFF-3 (light gray lines and triangles; 36.9°N, 100.6°W) from 12 to 14 Jun 2002.

the large scale (defined as scales larger than hundred of kilometers) that do not vary with time. There is a maximum (Fig. 4a) to the southeast corresponding to an area with a different land use (shrub) and a minimum in the northwest intensifying through the period as little precipitation is received. At smaller scales, the spatial heterogeneity of Ef (Figs. 4a–c) reflects both the transient heterogeneity of soil moisture whose fluctuations are linked to precipitation events (correlation between Ef and soil moisture is 0.44, 0.52, 0.35, respectively, for 12, 13, and 14 June) and the fixed heterogeneity of soil textures (cf. Fig. 4f). The Ef maxima correspond to areas that received the most rainfall: Ef patterns are strongly linked to the most recent precipitation pattern. Nevertheless, the heterogeneity in surface fluxes due to the heterogeneity in soil moisture is reduced 1 day after the rainfall, consistently with observations at ISFF. The impact of distinct soil textures on Ef can be seen at small scales. In fact, on 13 June, sandy soils located in the east received some rain and they correspond to a relative maximum of Ef, whereas in the domain's northwestern region, which did not receive rain, sandy soils correspond to a stronger Ef minimum. On 14 June, the soil texture (Fig. 4c) signatures are less marked in Ef in the east, as sandy soils display the largest decrease in Ef from 13 to 14 June.

c. *The observed 14 June mesoscale water vapor gradient*

1) MODIS DATA

Figures 8a,b shows the MODIS PW aggregated to a grid of 17.5 km × 22.5 km at 2340 LDT 11 June and at 1305 LDT 14 June. A mesoscale gradient is visible on both days. On 11 June the atmosphere is moister in the southeast (maximum value of 35.5 kg m^{-2}) and drier in the northwest (minimum value of 14.1 kg m^{-2}). This gradient is a typical climatological feature (Fig. 8c). On 14 June, a different mesoscale gradient is observed, with moister air in the southwest (maximum value of 36.5 kg m^{-2}) and drier air on the northeast (minimum value of 13 kg m^{-2}). This mesoscale gradient is mostly accounted for by the low-level water vapor gradient as assessed by sounding and aircraft data presented in the following sections. This is also consistent with the MODIS water vapor retrieval for 920 hPa, which is closely correlated with variations in PW ($r^2 = 0.92$).

2) SOUNDING DATA

Thirty-five soundings were launched during 14 June in a 200 × 200 km^2 zone around the Homestead profiling site. The range of variability in the mixing ratio as

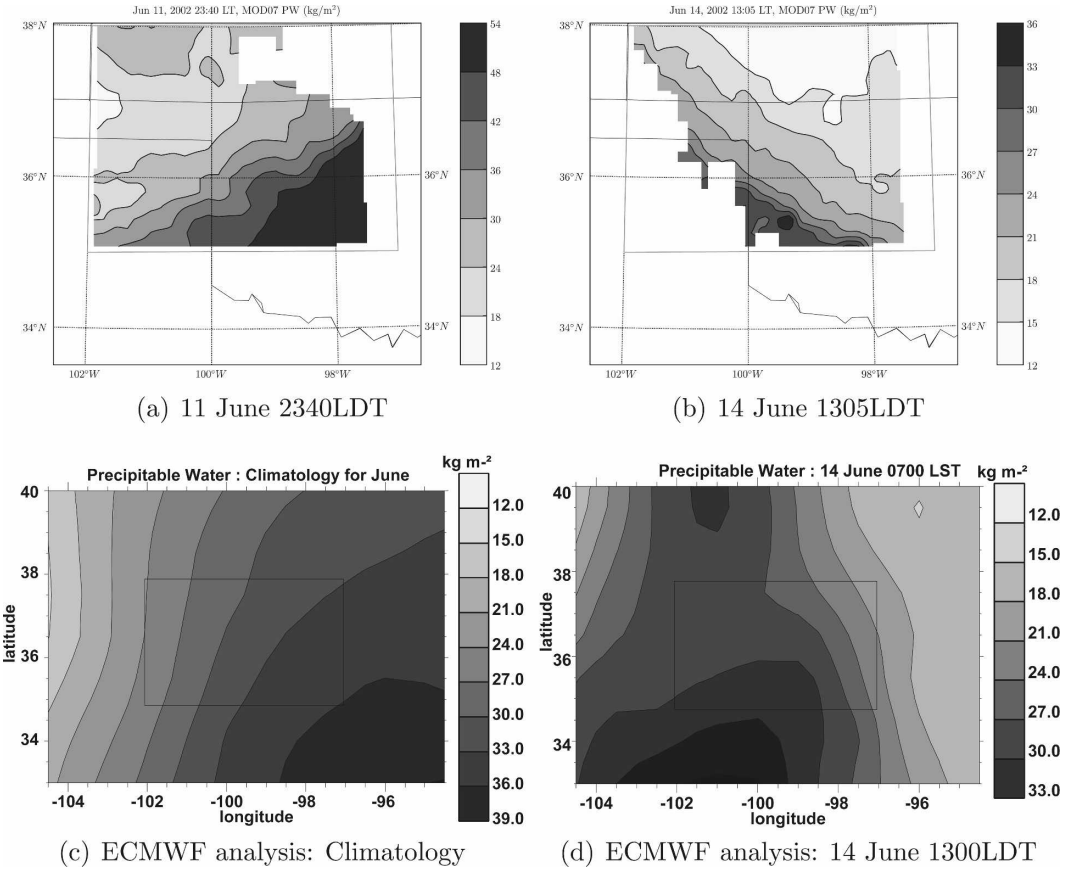

(a) 11 June 2340LDT (b) 14 June 1305LDT

(c) ECMWF analysis: Climatology (d) ECMWF analysis: 14 June 1300LDT

FIG. 8. PW from MODIS (resolution of 17.5 km × 22.5 km) (a) at 2340 LDT 11 Jun 2002 and (b) at 1305 LDT 14 Jun 2002 and from ERA40 analysis (resolution 0.5°), (c) for the climatological (1992–2002) June month, and (d) at 0700 LDT 14 Jun 2002. The squares in (c) and (d) correspond to the outlined domain in (a) and (b).

measured by soundings launched between 1200 and 1230 LDT, was 5.5 g kg^{-1} in the BL and 4 g kg^{-1} in the free troposphere (C05, see their Fig. 3). The northeasternmost sounding [Dodge City, Kansas (DDC), in Fig. 1] is the driest, with a mean water vapor mixing ratio of 5.5 g kg^{-1} (also lower PW value; Fig. 2), whereas the southwesternmost sounding [Amarillo, Texas (AMA)] is the moistest, with a mean water vapor mixing ratio of 11 g kg^{-1} (also larger PW in Fig. 2). This is consistent with the horizontal gradient sampled by the aircraft flight described below. Note that this gradient is already present in early-morning hours as assessed by the range of variability in the soundings (Fig. 6), about 4 g kg^{-1} in the low levels.

3) P-3 AND FALCON FLIGHT TRACKS

In situ data from the P-3 confirm the existence of a q gradient in the PBL at this scale. This aircraft flew at a height of around 350 m on successive legs, each approximately 80 km long oriented west-southwest–east-northeast. The gradient is 2 g kg^{-1} over 80 km at 0700 LDT and up to 3 g kg^{-1} at 1230 LDT (cf. C05, see their Fig. 4).

The DLR differential absorbing lidar (DLR-DIAL) data also indicates mesoscale variability of several grams per kilogram in q over hundred of kilometers for 14 June 2002. Strong lidar reflectivities indicate shallow convection in the southwest (over moister BL), but only much later in the northeast (drier BL).

Below we investigate the origin of the 14 June variability using the methodology presented in section 2, focusing on the respective role of surface fluxes and heterogeneity of the atmosphere on the observed mesoscale gradient.

4. Mesoscale variability

The mesoscale variability of boundary layer height and water vapor predicted by the 1D BL model is investigated first along the flight tracks and then over the broader 1D BL model domain.

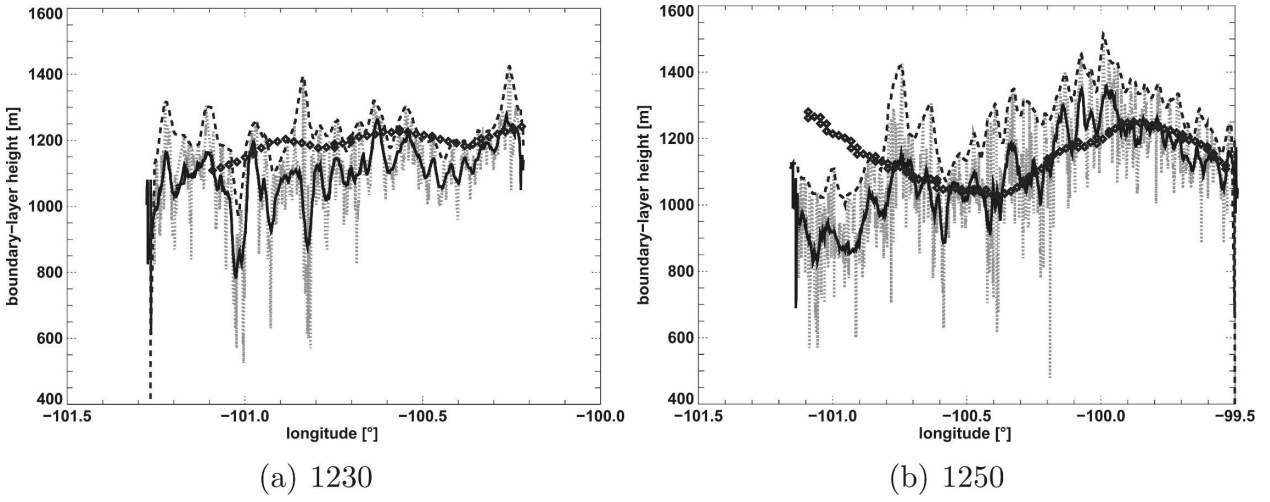

FIG. 9. Comparison of the boundary layer height predicted by the model (dark gray diamonds, 4-km resolution) with boundary layer heights deduced from lidar reflectivity profiles at 1230 and 1250 LDT along the respective flight tracks "a" and "b" noted in Fig. 1 (dotted gray, 75-m resolution; black line for 4-km smoothed signal; dashed black for the 4-km maximum).

a. Along the flight tracks

1) BOUNDARY LAYER HEIGHT

The boundary layer height derived from DLR-DIAL reflectivity data (following Davis et al. 2000) displays a superposition of scales of variability (Fig. 9). The variability at the submesoscale is linked to organized boundary layer structures, specifically thermals and dry tongues (C05; C07) and is outside the scope of this paper. Figure 9 shows the boundary layer height predicted by the BL model at 4-km resolution, h_m compared to the 4-km running mean (shown as the black full line, with the maximum as dashed black) of the DLR-DIAL estimate along two tracks, indicated in Fig. 1, at 1230 and 1250 LDT. There is general agreement between the predicted and observed mesoscale variation. Note that the boundary layer height is overestimated west of −100.7°W on track "b." The lidar cross section indicates the presence of shallow cumulus in the western end of the domain with cloud depths of about 200 m. This might explain the disagreement because (i) the existence of cumuli causes uncertainties in the derivation of boundary layer height from lidar reflectivities and (ii) our methodology takes into account clouds only through their radiative impacts at the surface (i.e., not on BL dynamics). The BL model also neglects advection including subsidence, which introduces additional uncertainty. C05 estimated the maximum subsidence to be about 1 cm s^{-1}, corresponding to an underestimate of about 200 m in the boundary layer height at 1230 LDT.

2) WATER VAPOR MIXING RATIO

The water vapor mixing ratio observed by the P-3 is also compared to the boundary layer water vapor mixing ratio predicted by the BL model, q_m, as shown in Fig. 10, on a 75-km leg at 1230 LDT. The q_m gradient is consistent with the observed gradient albeit with a smaller value of about 1 g kg^{-1} (75 km)$^{-1}$ instead of the observed 2.5 g kg^{-1} (75 km)$^{-1}$. The observed variability is also larger, which is expected given that the slab model does not reproduce the submesoscale variability resulting from the BL structures. As discussed below, the underestimate of the mesoscale gradient is partly explained by the neglect of advection. Another possible source of difference is the soil moisture: in TMI soil moisture (Fig. 4b), a decrease is observed eastward along this track whereas HRLDAS for this particular track shows large soil moisture fluctuations without an eastward decrease, except at the far eastern side of the track (see Fig. 11c). This leads to a different partitioning of the energy inbetween latent and sensible heat flux. In this case, greater latent heat flux and smaller sensible heat flux will induce a moister BL through a larger moisture influx in a less diluted boundary layer.

To understand the causes of the observed mesoscale variability, in Fig. 11 we show the variability of different variables along the flight tracks: the early-morning MM5 water vapor content q_o (the initial profile averaged over the mean boundary layer height, h), the simulated boundary layer height, and the HRLDAS surface heat flux and soil moisture. The model gradient of q_m over the track is well correlated with the gradient

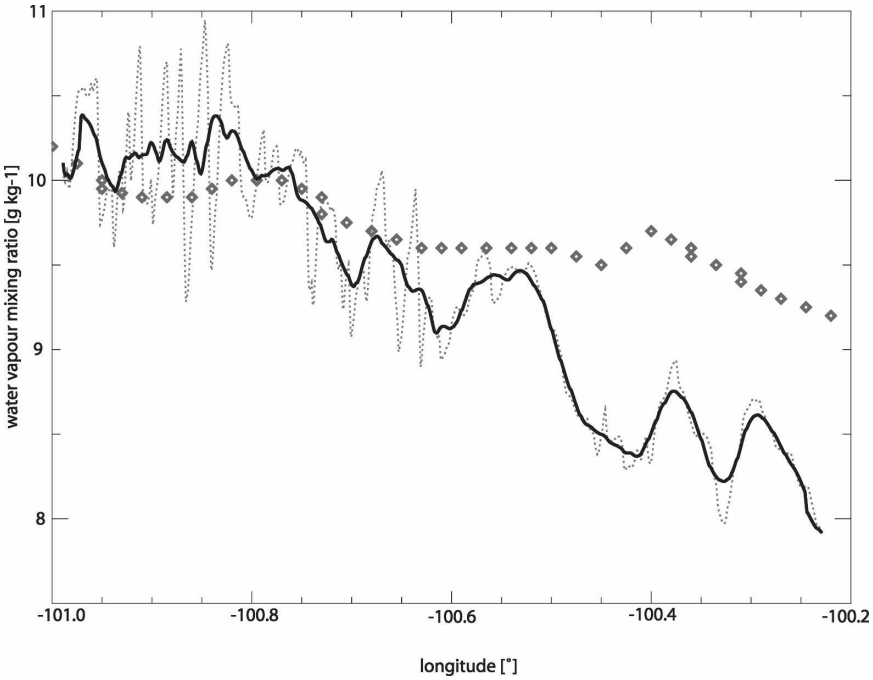

FIG. 10. Comparison of the boundary layer water vapor mixing ratio predicted by the model (dark gray diamonds, 4-km resolution) along the P-3 flight track with in situ aircraft measured values (dashed gray, 130-m resolution and black line for the 4-km smoothed signal) at 1230 LDT.

in q_o especially for the segment at 1230 LDT (Fig. 11a). Nevertheless, there is more variability in q_m than in q_o as suggested by variability at scales of a few tens of kilometers. At these scales, q_m fluctuations are well correlated with the inverse of h_m (Figs. 11d,h; $r^2 > 0.65$), with higher values for smaller boundary layer heights consistent with less dilution. Both q_m and LE (not shown) are not well correlated for the 1230 LDT track, with lower fluxes to the west and larger fluxes to the east. This is mainly due to the gradient of the total surface fluxes (with lower values to the southwest and higher values to the northeast; Fig. 4e). The evaporative fraction and the soil moisture fluctuations (Figs. 11b,c,f,g) are better correlated with q_m fluctuations. The variability at scales of a few tens of kilometers is linked to the boundary layer height and the variability of surface characteristics (Ef and soil moisture). This is in agreement with LES results of Avissar and Schmidt (1998) or Couvreux (2005) showing that the impact of surface flux heterogeneities on water vapor variability was significant from scales of 10 km.

The flight track analysis has underscored the role played by the initial spatial heterogeneity in determining the water vapor gradient. In addition, while the initial heterogeneity of the atmosphere accounts for the large-scale q gradient, the smaller-scale fluctuations are generated by both BL characteristics and surface heterogeneity (e.g., soil moisture and surface fluxes). An example of this is the good correlation between q_m and the inverse of the boundary layer height and to a lesser extent Ef and soil moisture. Observations also indicate a correlation between fluctuations in water vapor mixing ratio and lidar-derived boundary layer height. This suggests that the water vapor variability results from interactions between the early-morning heterogeneity of the atmosphere, the surface fluxes, and the boundary layer height. Small-scale variability (at a few tens of kilometers) develops with time in the BL model, but the mesoscale gradient does not increase as observed.

b. Role of advection

We have shown above that the daytime convective development from the early-morning atmospheric conditions leads to a mesoscale water vapor gradient in the BL. Nevertheless, its strength is underestimated compared to aircraft observations. ERA-40 reanalysis suggests strong advection of dry air from the northerly flow. Here, we investigate the role of horizontal advection as a possible cause for the increase of the gradient. C05 found that in the southwestern end of the "a" flight

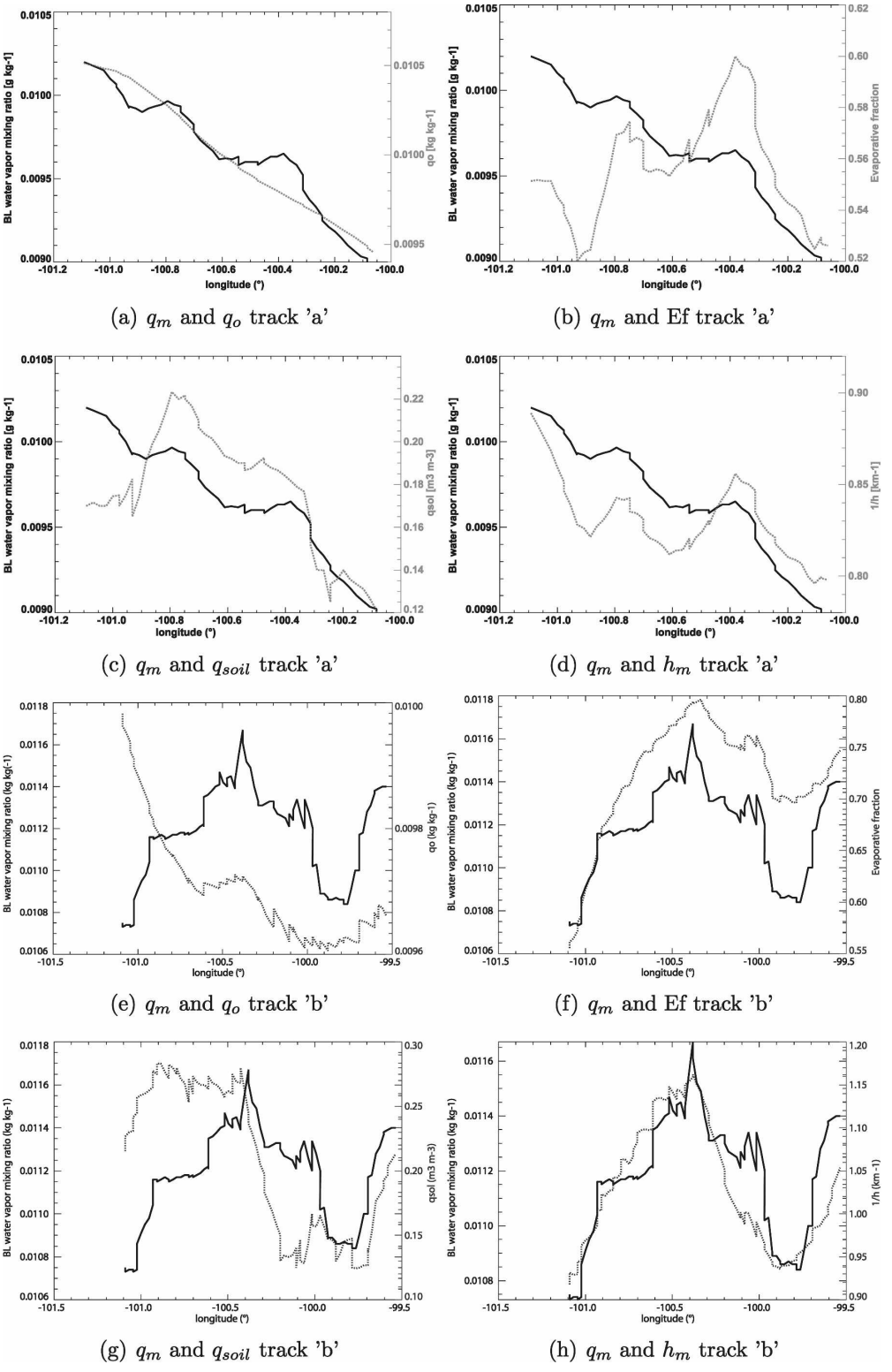

FIG. 11. Comparison of fluctuations along the two flight tracks of Fig. 8 for q_m, the BL model water vapor mixing ratio (black) and (dashed gray) (a), (e) q_o, the initial water vapor mixing ratio integrated over the mean boundary layer height; (b), (f) Ef; (c), (g) soil moisture; and (d), (h) the inverse of the BL height.

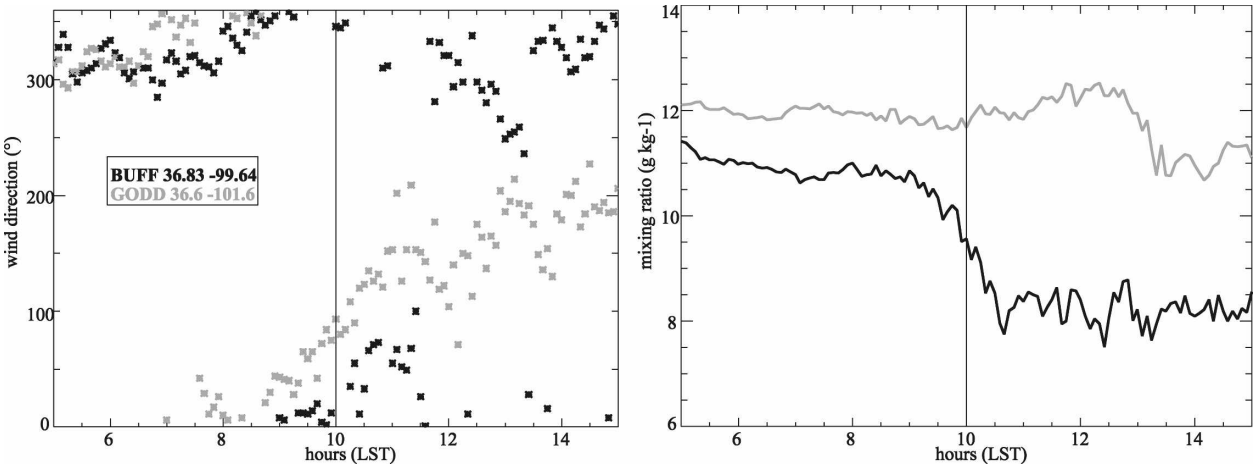

FIG. 12. Evolution of the (a) wind direction and (b) water vapor mixing ratio for two Oklahoma Mesonet stations (5-min resolution) on each side of the aircraft transect, BUFF (black) to the northeast in black and GODD (gray) to the southwest.

track, q remains approximately constant whereas in the northeastern end it decreases strongly with time (see their Fig. 4). C05 also showed that moisture advection occurs at scales greater than 10 km and was significant below 3000 m with a value of 0.1 to 0.15 g kg^{-1} h^{-1}.

The Oklahoma Mesonet provides surface data close to the flight track at Buffalo (BUFF: 36.83°N, −99.64°W) and Goodwell (GODD: 36.6°N, −101.6°W). As indicated in Fig. 12a, prior to 1000 LDT, the northerly wind direction is similar at both stations. After 1000 LDT, the wind veers at GODD, becoming southerly whereas the wind direction at BUFF stays roughly constant (the wind speed at both stations is about 3 m s^{-1}). This change of wind direction, consistent with aircraft measurement, is related to the displacement of the high pressure center. Given the gradient described above or obtained from the Oklahoma mesonet (about 1.5 g kg^{-1} in 140 km) the horizontal advection will bring moister air to GOOD and tend to dry the boundary layer at BUFF. Even though the wind speeds are relatively small, the existence of a strong gradient and opposing wind directions can produce horizontal advection that can lead to an increase of this gradient due to a decreasing (increasing) of q in the northeastern (southwestern) end. This partly explains the increase in the q difference between these two stations from 1000 to 1300 LDT (Fig. 12b).

c. *Spatial structures*

After examining the variability of the boundary layer height and water vapor along one direction (the flight tracks) we now focus on the different causes of the spatial variability in the BL model domain.

1) COMPARISON TO MODIS PRECIPITABLE WATER

Spatial structures of q_m and the MODIS PW are presented in Figs. 13a,b. Both show the large-scale gradient with higher values in the southwest and lower values in the northeast. This gradient is primarily due to the initial heterogeneity of the atmosphere as shown by the map of q_o (Fig. 13c) at 1300 LDT (at this time, the mean boundary layer height is about 1100 m). However, differences are evident between the q_m and q_o heterogeneities: for example, in the southeast, q_m is relatively higher due to strong LE (see Ef in Fig. 4a). In addition, the spatial structure of q_m evolves from a field organized along a preferred direction (Fig. 13c) to a field presenting more variability along both directions and at smaller scales: for example, note the bulges at (37°N, 100°W) and (36.5°N, 97°–98°W) both in q_m and PW, consistent with the small-scale variability developed throughout the day along the flight track. Thus, although the early-morning heterogeneity explains the mesoscale water vapor variability to first order at the largest scales, other factors shape the variability at smaller scales.

In the following, we investigate how the initial mesoscale gradient is modified by the boundary layer development and the heterogeneity of surface fluxes.

2) ROLE OF HETEROGENEOUS SURFACE FLUXES

The boundary layer height simulated by the BL model at 1300 LDT displays large variations from 650 up to 1800 m with a mean value of 1100 m (Fig. 14a). These variations are driven primarily by the spatial variation in surface buoyancy flux (r^2 = 0.6). This is

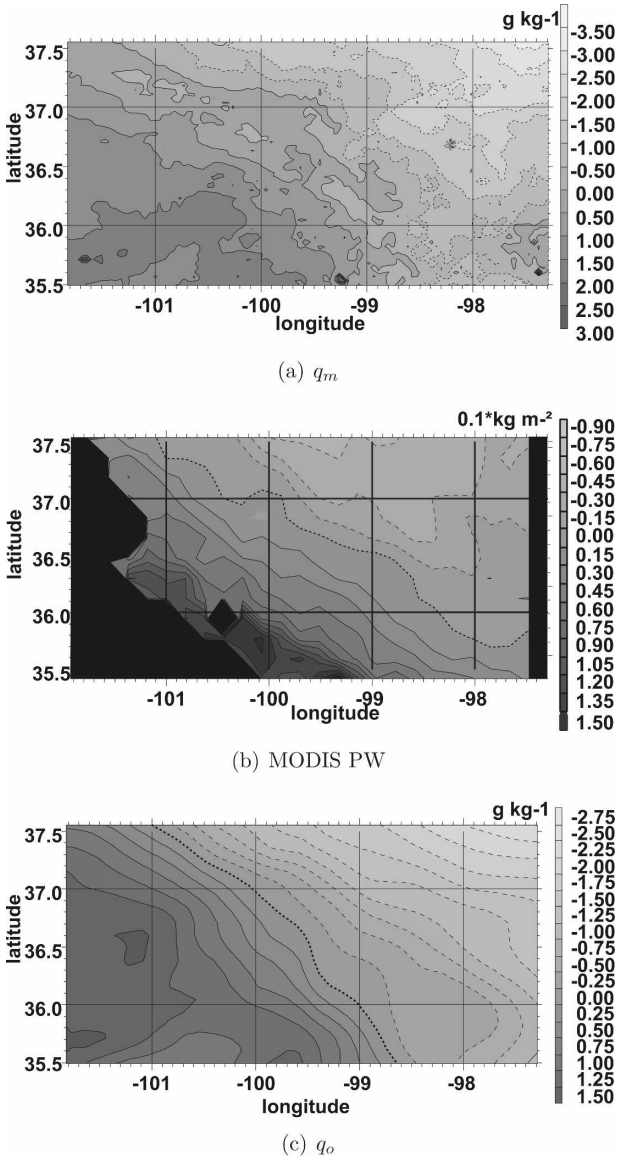

FIG. 13. Maps of (a) q_m predicted by the 1D BL model, (b) PW measured by MODIS, and (c) q_o, the early-morning water vapor mixing ratio averaged over the mean boundary layer height at 1300 LDT 14 Jun 2002 (all fields are presented in anomaly relatively to the mean over the domain). The black zones in (b) correspond to the area with no data.

particularly the case in the northwest (latitude $>$ 36.5°N and longitude < -100°W) where r^2 reaches 0.9. In the northwest, HRLDAS simulates very dry soils and high buoyancy fluxes. However, there is little correlation over the whole domain between the time-integrated buoyancy fluxes and the surface soil moisture ($r^2 = 0.23$), at the 4-km scale considered, in contrast to the strong correlation found in this area during the Southern Great Plains 1997 field study (Desai et al. 2006). They found the highest correlation for scales about 100 km; we note that at the 40-km scale, the correlation is higher ($r^2 = 0.39$). The correlation between Ef and soil moisture is slightly larger, ($r^2 = 0.36$ at the 4-km scale). In fact, dividing the sensible heat flux by LE + H essentially normalizes H by Rnet (there could also be a change in flux into the soil, G, but ISFF data suggest a ratio of about 1/5 between horizontal variation of Rnet and G). This Rnet variation can also explain the differences between the flux and soil moisture correlations in the two cases; Desai et al. (2006) studied clear-sky days for which there was relatively little variation in Rnet.

We also considered variations in the early-morning atmospheric stratification through fluctuations in lapse rate in the initial profiles, from 4.8 to 5.6 K km^{-1}, as a source of variability. A similar range of lapse-rate fluctuations is observed throughout the soundings on 14 June 2002. This variability is only moderately correlated with fluctuations in boundary layer height ($r^2 = 0.35$). Differences at 1300 LDT between h_m and h_o (boundary layer height computed from a spatially homogeneous atmosphere) were smaller than 200 m west of -98.5°W (Fig. 14b), confirming that in the west the buoyancy flux (and not the spatially varying stability) is the primary driver of the boundary layer height ($r^2 = 0.85$ for the correlation of h_m and buoyancy flux west of -98.5°W compared with $r^2 = 0.52$ east of -98.5°W). In the east, in contrast, the atmospheric stratification plays a significant role in boundary layer fluctuations. To summarize, the early-morning stratification of the atmosphere is the determinant for the boundary layer water vapor variability but less so for the boundary layer height.

To investigate the role of surface fluxes on the water vapor variability, we focus on the difference between q_m computed by the BL model and q_0, defined as the initial water vapor mixing ratio averaged over the mean boundary layer height. As illustrated for 1300 LDT by Figs. 14a,c,d, spatial heterogeneities in the deviation from the initial water vapor content of the atmosphere are driven both by variations in h_m ($r^2 = 0.48$) and variations in Ef ($r^2 = 0.55$). The correlation between $q_m - q_o$ and LE is less important ($r^2 = 0.25$), underlining the role of Rnet variations. Nevertheless, Ef and h_m are not independent (as h_m is primarily driven by the surface buoyancy fluxes). The increase of Ef can be due to an increase in LE and/or a decrease in H. Both will contribute to an increase of the boundary layer q due to a larger influx of moisture and/or to less dilution by the boundary layer growth.

With time, the surface flux heterogeneities introduce smaller-scale variability to the BL q field, through Ef and h_m (Fig. 14c). This underscores the point that the

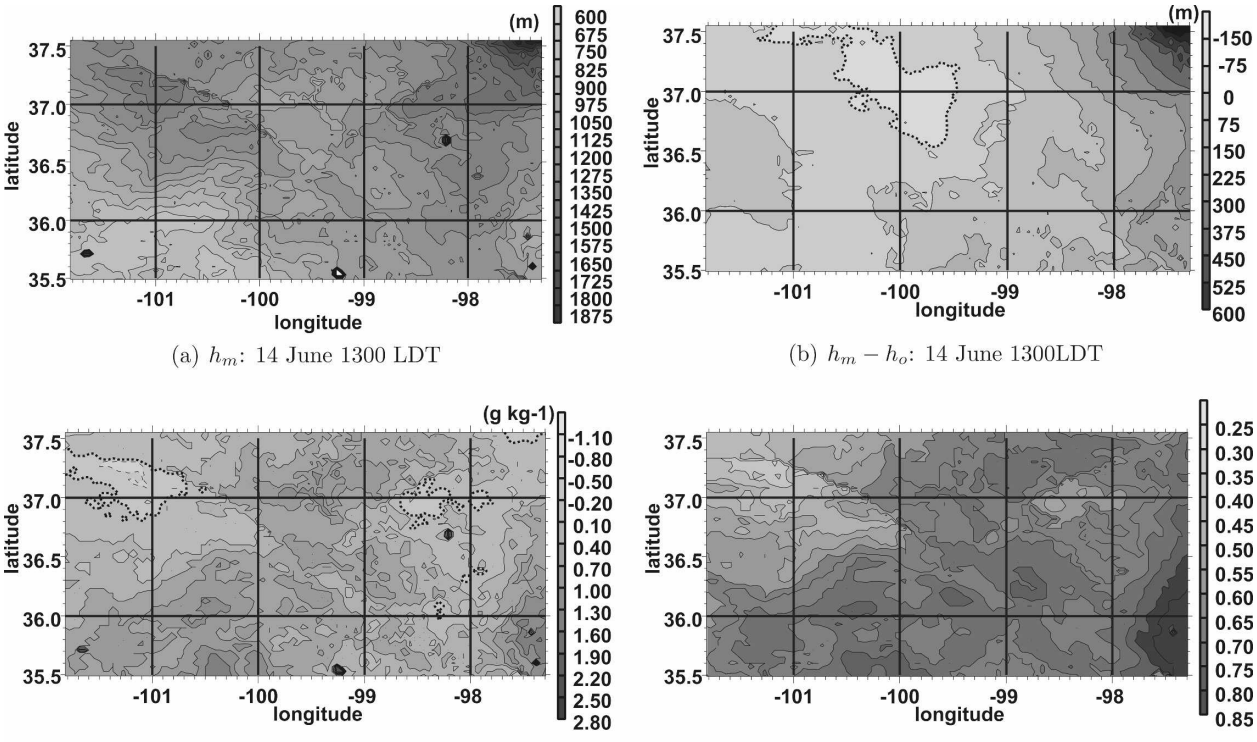

(a) h_m: 14 June 1300 LDT

(b) $h_m - h_o$: 14 June 1300LDT

(c) $q_m - q_o$:14 June 1300LDT

(d) Cumulative EF

FIG. 14. Spatial fluctuations of (a) BL height, (b) BL height with minus BL height without initial atmospheric heterogeneity, (c) BL water vapor mixing ratio minus initial water vapor mixing ratio integrated over the mean boundary layer height, and (d) cumulative Ef from 0600 to 1300 LDT 14 Jun 2002.

mesoscale variability of water vapor results from the combination of variability in boundary layer height, latent heat flux, and early-morning heterogeneity of the atmosphere and variations of horizontal moisture advection. Rnet fluctuates significantly over the domain (Fig. 4e): H + LE spans the range (200–450 W m^{-2}) when averaged over the day (from 0600 to 1800 LDT). These fluctuations are due to clouds present in the southwest as attested by lidar measurements and the MODIS cloud mask. These variations in Rnet induce larger variations in the sensible heat flux and tend to strengthen the initial q gradient along the flight track through smaller BL height.

5. Conclusions

Mesoscale water vapor heterogeneities in the boundary layer on 14 June 2002 have been studied within the context of the IHOP_2002 field campaign. During this day, a strong mesoscale water vapor gradient was observed by different instruments deployed in the boundary layer (e.g., aircraft, radiosondes, and DIAL). MODIS was shown to provide observations relevant to the evaluation of the mesoscale variability of water vapor, since most of the satellite-observed PW fluctuations arose from low-level water vapor mixing ratio fluctuations. This northeast–southwest gradient stood in contrast to the characteristic northwest–southeast gradient expected from climatology.

We have investigated the respective roles of early-morning heterogeneity in the atmosphere and heterogeneities in surface fluxes on the daytime evolution of mesoscale variability of boundary layer height and water vapor. To do so, we used a 1D boundary layer model (a mixed layer model) in conjunction with a high-resolution land data assimilation system that provides a valuable estimate of surface fluxes at mesoscale. This enables us to distinguish the impact of spatial heterogeneities in surface fluxes from the impact of heterogeneities in the early-morning stratification. Spatial heterogeneities in boundary layer height are primarily driven by variability in the surface buoyancy fluxes. On 14 June, this is particularly true west of −98.5°W. East of −98.5°W, the stratification of the atmosphere also plays a significant role. For this day, the buoyancy fluxes were not strongly correlated to soil moisture (especially at small scales) but were more directly controlled by net radiation. Daytime boundary layer water

vapor displays variability at different scales that results from interactions between surface latent heat flux, boundary layer height, and the early-morning heterogeneity of the atmosphere, with a spatially varying combination of processes. Horizontal advection also plays a significant role. This complexity underscores the fact that the evolving spatial heterogeneity of daytime boundary layer water vapor is related not only to surface characteristics, but also depends on the early-morning atmospheric profiles at synoptic scales, consistent with the findings of Findell and Eltahir (2003). On 14 June, the initial heterogeneity in the atmosphere largely accounts for the water vapor gradient at large scales. This heterogeneity likely results from horizontal advection and modification of the atmosphere by moist convection occurring on previous days. Variability at smaller scales is more closely related to boundary layer height and evaporative fraction patterns and is therefore related to the surface flux heterogeneities.

We have shown through this case study that the use of a 1D model fed by inputs from a SVAT for surface fluxes and a mesoscale analysis is a useful tool to help in the interpretation of field campaign observations. In comparison to a mesoscale model, which integrates the effect of many processes, this approach has the ability to separately evaluate the impact of individual processes. This methodology can also be used to qualitatively evaluate a land data assimilation system, given that a more direct surface flux validation is very difficult because of the lack of observations and representativeness issues.

Acknowledgments. The authors thank K. Craig for the retrieval of boundary layer depths from lidar data and B. Geerts for KA data. This research has been supported by the GAME (CNRS-Météo-France). We acknowledge the support from the National Center for Atmosperic Research (NCAR) Water Cycle Across Scale Program at The Institute for Integrative and Multidisciplinary Earth Studies (TIIMES), the (National Science Foundation) NSF/NCAR U.S. Weather Research Program (USWRP), NASA-THP (Dr. Jared Entin NNG06GH17G), the NASA-GWEC (NNG05GB41G), and the Canadian Foundation for Climate and Atmospheric Science. The authors also thank the reviewers for their helpful comments that considerably improved the manuscript.

APPENDIX

The Mixed Layer Slab Model

The time evolution of the boundary layer height is given by Garratt's (1994) Eq. (6.21):

$$h(t)^2 = h(t-1)^2 + 2 \times \frac{(1+2c)}{\gamma} \int_{t-1}^{t} \overline{w'\theta'_{\upsilon \mathrm{sf}}}\, dt'. \quad \text{(A1)}$$

This formulation takes into account the impact of water vapor on the growth of the boundary layer through the use of the surface buoyancy flux. The lapse rate (γ) is the mean lapse rate between the previous boundary layer height at the previous time $h(t-1)$ and the new one $h(t)$. In this model, subsidence and any contribution of mechanical turbulence are neglected. The latter assumption requires that winds are moderate and for this reason this model should not be used just after sunrise, where shear plays a significant role in the development of the boundary layer. Here, we focus primarily on 1200 LDT and on a day (14 June) with a wind speed less than 5 m s^{-1}. We do however begin the model spinup at 0800 LDT. The model is then run for 7 h.

The time evolution of the boundary layer water vapor mixing ratio is obtained by a simple scaling formulation:

$$q_m(t) = \frac{1}{h(t)} \times \left[q_m(t-1) \times h(t-1) + \int_{h(t-1)}^{h(t)} q_i(z)\, dz + \int_{t-1}^{t} \overline{w'q'_{\mathrm{sf}}}\, dt' \right]. \quad \text{(A2)}$$

This approaches uses the vertical structure of the water vapor mixing ratio profile, as opposed to an analytical profile (e.g., assuming an exponential decrease), which would smooth the impact of any early-morning atmospheric vertical heterogeneity.

REFERENCES

Alapaty, K., S. Raman, and D. S. Niyogi, 1997: Uncertainty in the specification of surface characteristics: A study of prediction errors in the boundary layer. *Bound.-Layer Meteor.,* **82,** 473–500.

André, J. C., P. Bougeault, and J.-P. Goutorbe, 1990: Regional estimates of heat and evaporation fluxes over non-homogeneous terrain. Examples from the HAPEX-MOBILHY program. *Bound.-Layer Meteor.,* **50,** 77–108.

Anthes, R. A., 1984: Enhancement of convective precipitation by mesoscale variations in vegetative covering in semiarid regions. *J. Climate Appl. Meteor.,* **23,** 541–554.

Avissar, R., and T. Schmidt, 1998: An evaluation of the scale at which ground-surface heat flux patchiness affects the convective boundary layer using large-eddy simulations. *J. Atmos. Sci.,* **55,** 2666–2689.

Betts, A. K., 2004: Understanding hydrometeorology using global models. *Bull. Amer. Meteor. Soc.,* **85,** 1673–1688.

——, and C. Jakob, 2002: Study of diurnal cycle of convective precipitation over Amazonia using a single column model. *J. Geophys. Res.,* **107,** 4732, doi:10.1029/2002JD002264.

Brotzge, J. A., and K. C. Crawford, 2003: Examination of the surface energy budget: A comparison of eddy-correlation and

Bowen-ratio measurement systems. *J. Hydrometeor.,* **4,** 160–178.

Chen, F., T. Warner, and K. Manning, 2001: Sensitivity of orographic moist convection to landscape variability: A study of the Buffalo Creek, Colorado, flash-flood case of 1996. *J. Atmos. Sci.,* **58,** 3204–3223.

——, and Coauthors, 2007: Description and evaluation of the characteristics of the NCAR high-resolution Land Data Assimilation System during IHOP-02. *J. Appl. Meteor. Climatol.,* **46,** 694–713.

Couvreux, F., 2005: Water vapor variability in the convective boundary layer. Ph.D. dissertation, University of Toulouse, Toulouse, France, 194 pp.

——, F. Guichard, J.-L. Redelsperger, C. Kiemle, V. Masson, J.-P. Lafore, and C. Flamant, 2005: Water vapour variability within a convective boundary layer assessed by Large Eddy Simulations and IHOP_2002 observations. *Quart. J. Roy. Meteor. Soc.,* **131,** 2665–2693.

——, ——, V. Masson, and J.-L. Redelsperger, 2007: Negative water vapour skewness and dry tongues in the convective boundary layer: Observations and large-eddy simulation budget analysis. *Bound.-Layer Meteor.,* **123,** 269–294.

Crook, N. A., 1996: Sensitivity of moist convection forced by boundary-layer processes to low-level thermodynamics field. *Mon. Wea. Rev.,* **124,** 1767–1785.

Davis, K. J., N. Gamage, C. Hagelberg, D. H. Lenschow, C. Kiemle, and P. P. Sullivan, 2000: An objective method for determining atmospheric structure from airborne lidar observations. *J. Atmos. Oceanic Technol.,* **17,** 1455–1468.

Desai, A. R., K. J. Davis, C. J. Senff, S. Ismail, E. V. Browell, D. R. Stauffer, and B. P. Reen, 2006: A case-study on the effects of heterogeneous soil moisture on mesoscale boundary-layer structure in the Sounthern Great Plains, U.S.A. I: Simple prognostic model. *Bound.-Layer Meteor.,* **119,** 195–238.

Dodd, A. V., 1965: Dew point distribution in the contiguous United States. *Mon. Wea. Rev.,* **93,** 113–122.

Drusch, M., and P. Viterbo, 2007: Assimilation of screen-level variables in ECMWF's Integrated Forecast System: A study on the impact on the forecast quality and analyzed soil moisture. *Mon. Wea. Rev.,* **135,** 300–314.

Findell, K. L., and E. A. B. Eltahir, 2003: Atmospheric controls on soil moisture–boundary layer interactions. Part I: Framework development. *J. Hydrometeor.,* **4,** 552–569.

Gao, H., E. F. Wood, T. J. Jackson, M. Drusch, and R. Bindlish, 2006: Using TRMM/TMI to retrieve surface soil moisture over the southern United States from 1998 to 2002. *J. Hydrometeor.,* **7,** 23–38.

Garratt, J. R., 1994: *The Atmospheric Boundary Layer.* Cambridge University Press, 334 pp.

Grell, G. A., J. Dudhia, and D. R. Stauffer, 1995: A description of the V generation Penn State/NCAR mesoscale model (MM5). Tech. Rep., National Center for Atmospheric Research, 121 pp.

Holt, T., D. Niyogi, F. Chen, K. Manning, M. A. LeMone, and A. Qureshi, 2006: Effect of land–atmosphere interactions on the IHOP 24–25 May 2002 convection case. *Mon. Wea. Rev.,* **134,** 113–133.

Kang, S.-L., K. J. Davis, and M. LeMone, 2007: Observations of the BL structures over a heterogeneous land surface during IHOP_2002. *J. Hydrometeor.,* **8,** 221–244.

King, M. D., and Coauthors, 2003: Cloud and aerosol properties, precipitable water, and profiles of temperature and water vapor from MODIS. *IEEE Trans. Geosci. Remote Sens.,* **41,** 442–458.

LeMone, M. A., and Coauthors, 2007: NCAR/CU surface, soil, and vegetation observations during the International H_2O Project 2002 Field Campaign. *Bull. Amer. Meteor. Soc.,* **88,** 65–81.

Mahrt, L., 1991: Boundary-layer moisture regimes. *Quart. J. Roy. Meteor. Soc.,* **117,** 151–176.

——, 2000: Surface heterogeneity and vertical structure of the boundary layer. *Bound.-Layer Meteor.,* **96,** 33–62.

Milford, J. R., S. Abdulla, and D. A. Mansfield, 1979: Eddy flux measurements using an instrumented powered glider. *Quart. J. Roy. Meteor. Soc.,* **105,** 673–693.

Pielke, R. A., 2001: Influence of the spatial distribution of vegetation and soils on the prediction of cumulus convective rainfall. *Rev. Geophys.,* **39** (2), 151–177.

Rabin, R. M., S. Stadler, P. J. Wetzel, D. J. Stensrud, and M. Gregory, 1990: Observed effects of landscape variability on convective clouds. *Bull. Amer. Meteor. Soc.,* **71,** 272–280.

Raupach, R. R., and J. J. Finnigan, 1995: Scale issues in boundary-layer meteorology: Surface energy balances in heterogeneous terrain. *Hydrol. Proc.,* **9,** 589–612.

Seemann, S. W., W. Li, P. Menzel, and L. E. Gumley, 2003: Operational retrieval of atmospheric temperature, moisture, and ozone from MODIS infrared radiances. *J. Appl. Meteor.,* **42,** 1072–1091.

Stirling, A. J., and J. C. Petch, 2004: The impacts of spatial variability on the development of convection. *Quart. J. Roy. Meteor. Soc.,* **130,** 3189–3206.

Stull, R. B., 1988: *An Introduction to Boundary Layer Meteorology.* Kluwer Academic Publishers, 666 pp.

Trier, S., F. Chen, and K. Manning, 2004: A study of convection initiation in a mesoscale model using high-resolution land surface initiation conditions. *Mon. Wea. Rev.,* **132,** 2954–2976.

Weckwerth, T. M., and Coauthors, 2004: An overview of the International H_20 Project (IHOP_2002) and some preliminary highlights. *Bull. Amer. Meteor. Soc.,* **85,** 253–277.

Wilson, J. W., and R. D. Roberts, 2006: Summary of convective storms initiation and evolution during IHOP: Observational and modeling perspective. *Mon. Wea. Rev.,* **134,** 23–47.

Wulfmeyer, V., H.-S. Bauer, M. Grzeschik, A. Behrendt, F. Vandenberghe, E. V. Browell, S. Ismail, and R. A. Ferrare, 2006: Four-dimensional variational assimilation of water vapor differential absorption lidar data: The first case study within IHOP_2002. *Mon. Wea. Rev.,* **134,** 209–230.